EurJIC
European Journal of Inorganic Chemistry

Research Article
doi.org/10.1002/ejic.202400124

Chemistry Europe
European Chemical Societies Publishing

www.eurjic.org

Role of Alkylated 2,6-bis(tetrazol-5-yl)pyridyl Ligands and Iron(II) Salts in Selecting Spin Crossover Complexes

Rita Mazzoni,*[a] Stefano Baratti,[b] Daniel Rustichelli,[b] Stefano Stagni,[a] Valentina Fiorini,[a] Stefano Zacchini,[a] Dawid Pinkowicz,[c] Alessandra Forni,[d] Jasper R. Plaisier,[e] Lara Gigli,[e] and Luca Rigamonti*[b]

The substituents in 2,6-bis(2-R-2*H*-tetrazol-5-yl)pyridyl neutral ligands R_2btp (R = Me, *t*Bu) revealed a prominent effect when reacting with iron(II) salts, in combination with the nature of the anion. According to metal:ligand molar ratio, reaction of R_2btp with $FeCl_2$ led to isolate $[Fe^{II}(R_2btp\text{-}\kappa^3N,N',N'')_2](Fe^{III}Cl_4)_2$, R = Me (**1 a**) and *t*Bu (**2 a**), where the octahedral iron(II) centres bring two tridentate ligands in *mer* coordination mode, but also $[Fe^{II}(tBu_2btp\text{-}\kappa^3N,N',N'')(tBu_2btp\text{-}\kappa N)_2(H_2O\text{-}\kappa O)](Fe^{III}Cl_4)_2$ (**2 b**), where one ligand is tridentate, while the other two coordinate the iron(II) through one tetrazolyl nitrogen atom, and the octahedral sphere is completed by one water molecule. In all cases, half of the iron ions are oxidised to iron(III) forming the paramagnetic tetrachloroferrato counterions. Reaction of tBu_2btp with $Fe(ClO_4)_2\cdot 6H_2O$ led to the octahedral $[Fe^{II}(tBu_2btp\text{-}\kappa^3N,N',N'')_2](ClO_4)_2\cdot 4DCM$ (**4 a**·4DCM), which shows solvent-dependent spin crossover behaviour: while **4 a**·4DCM is blocked in the high spin state, its unsolvated form, **4 a**, undergoes spin transition to low spin in two subsequent steps at 206 K, with opening of a 23-K hysteresis ($T_{1/2\downarrow}$ = 194 K, $T_{1/2\uparrow}$ = 217 K), and at 136 K ($T_{1/2\downarrow}$ = 135 K, $T_{1/2\uparrow}$ = 137 K). The magnetic profile changes to an incomplete spin transition when the sample absorbs water molecules yielding **4 a**·1.5H_2O.

Introduction

Spin crossover (SCO) materials, and especially the ones containing iron(II) centres, are among the most-studied compounds in the field of molecular magnetism.[1,2] They have been extensively investigated in the past years since the switch from low (LS) to high (HS) spin state can be reversibly controlled by external stimuli, like temperature, light, pressure, etc.,[3–5] thus holding promises for application in information processing and data storage devices or molecular switches.[6–10] Special interest has been focussed on compounds that show spin modulation upon light irradiation, with the so-called LIESST (Light-Induced Excited Spin State Trapping) effect at cryogenic temperatures, mostly studied in iron(II) complexes,[10–12] and upon application of external pressure, since it favours a LS configuration increasing the SCO transition temperature.[13] Another factor that shows an impact on the SCO properties in the solid state is the crystal packing, as given by the change of counterions, substituents on the donor ligands and/or the presence of crystallization solvent, since it changes the asset of iron(II) centres in the crystal structure.[14–18]

Variably-substituted 2,6-bis(pyrazol-1-yl)pyridyl (bpp) derivatives are well-known tridentate ligands able to coordinate iron(II) ions in a *mer* fashion yielding robust octahedral complexes of general formula $[Fe(bpp\text{-}\kappa^3N,N',N'')_2](X)_2$ (X^- = anion).[16,17,19] The strength of the crystal field generated by these two nitrogen donor ligands allows the metal centre to show thermally-induced SCO, but also stabilization of either LS ($S = 0$) or HS ($S = 2$) state upon subtle variation of the substituents on the ligand, as found for *para*-pyridyl-substituted complexes $[Fe(bpp\text{-}R\text{-}\kappa^3N,N',N'')_2](ClO_4)_2$.[19–22] The related 2,6-bis(2*H*-tetrazol-5-yl)pyridine (H_2btp)[23,24] tridentate ligand is structurally very similar to bpp derivatives, and it has already been applied in the synthesis of both *mer* heteroleptic metal complexes with ruthenium(II)[25,26] and platinum(II),[27] and some homoleptic examples with lanthanide ions[28] and 3*d* metals like cobalt(II), nickel(II), copper(II) and zinc(II),[29] together with one unique example with iron(II) with the dianionic homoleptic $(A)_2[Fe(btp)_2]$ derivatives (A^+ = ammonium cation).[30] There are also few neutral iron(II) complexes of general formula $[Fe(ptp)_2]$ with mixed pyrazolyltetrazolylpyridyl (Hptp) ligands, relevant for their SCO properties.[31,32]

In this work we decided to focus our attention on the neutral *N*2,*N*2-R_2btp derivatives (R = Me, *t*Bu), in which the

[a] *R. Mazzoni, S. Stagni, V. Fiorini, S. Zacchini*
Dipartimento di Chimica Industriale 'Toso Montanari', Università degli Studi di Bologna, Via Gobetti 85, 40129 Bologna, Italy
E-mail: rita.mazzoni@unibo.it

[b] *S. Baratti, D. Rustichelli, L. Rigamonti*
Dipartimento di Scienze Chimiche e Geologiche, Università degli Studi di Modena e Reggio Emilia, via G. Campi 103, 41125 Modena, Italy
E-mail: luca.rigamonti@unimore.it

[c] *D. Pinkowicz*
Faculty of Chemistry, Jagiellonian University, Gronostajowa 2, 30-387 Kraków, Poland

[d] *A. Forni*
Consiglio Nazionale delle Ricerche, Istituto di Scienze e Tecnologie Molecolari "G. Natta" (CNR-SCITEC), and INSTM RU of Milan, via C. Golgi 19, 20133 Milano, Italy

[e] *J. R. Plaisier, L. Gigli*
Elettra-Sincrotrone Trieste S.C.p.A, Strada Statale 14, Km 163.5, 34149 Basovizza, Trieste, Italy

Supporting information for this article is available on the WWW under https://doi.org/10.1002/ejic.202400124

Research Article
doi.org/10.1002/ejic.202400124

lateral tetrazolyl rings of H_2btp are alkylated by two methyl or *tert*-butyl groups on the farther nitrogen atoms (*N*2) with respect to the central pyridyl ring (to make reading easier, the *N*2,*N*2 prefix will be omitted in the following), leading to 2,6-bis(2-(methyl)-2*H*-tetrazol-5-yl)pyridine (Me_2btp)[26,33] or 2,6-bis(2-(*tert*-butyl)-2*H*-tetrazol-5-yl)pyridine (tBu$_2$btp), respectively. By reaction with iron(II) perchlorate we were aiming at obtaining the homoleptic hexacoordinated compounds [Fe(R_2btp-κ^3*N,N′,N″*)$_2$]$(ClO_4)_2$ analogous to bpp derivatives to study their magnetic properties, like modulated SCO behaviour given by the pyrazole-tetrazole substitution, but also the pentacoordinated species [$FeCl_2$(R_2btp-κ^3*N,N′,N″*)] by reaction with iron(II) chloride, to study their possible activity as valuable catalysts in analogy to iron(II) catalysts with 2,6-bis(imino)pyridyl ligands.[34,35] We discovered a rich reactivity exhibited by these ligands, highlighting the peculiar effects of both the R groups and the nature of the anions. In particular, in the case of $FeCl_2$ we obtained the compounds [Fe^{II}(R_2btp-κ^3*N,N′,N″*)$_2$]($Fe^{III}Cl_4$)$_2$, R = Me (**1a**) and *t*Bu (**2a**), but also [Fe^{II}(tBu$_2$btp-κ^3*N,N′,N″*)(tBu$_2$btp-κ*N*)$_2$(H_2O-κ*O*)]($Fe^{III}Cl_4$)$_2$ (**2b**) by modulating the metal:ligand molar ratio, where the chloride anion is never coordinated to iron(II) and partial oxidation to iron(III) always occurred to the tetrachloroferrato anions as preferred counterions even working under inert atmosphere, and revealing also the role of the substituent R of the ligand. When moving to perchlorate as iron(II) salt, we recently reported about the solvent-incorporating octacoordinated complex [Fe^{II}(Me_2btp-κ^3*N,N′,N″*)$_2$(CH_3CN-κ*N*)(H_2O-κ*O*)]$(ClO_4)_2 \cdot H_2O$ (**3b**·H_2O) as solid-state-trapped intermediate in the conversion of the mixed-spin HS-LS species [Fe^{II}(Me_2btp-κ^3*N,N′,N″*)$_2$]$(ClO_4)_2 \cdot$MeCN$\cdot 2.75H_2O$ (**3a**·MeCN·2.75H_2O) into [{Fe^{II}(Me_2btp-κ^3*N,N′,N″*)$_2$}{Fe^{II}(Me_2btp-κ^3*N,N′,N″*)(MeCN-κ*N*)$_2$(H_2O-κ*O*)}]$(ClO_4)_4 \cdot$MeCN (**3a**·**3c**·MeCN).[33] Conversely, the octahedral complex [Fe^{II}(tBu$_2$btp-κ^3*N,N′,N″*)$_2$]$(ClO_4)_2 \cdot$4DCM (**4a**·4DCM) (DCM = CH_2Cl_2) could be isolated when working with tBu$_2$btp. The synthetic conditions and molecular structures of all compounds obtained through single-crystal X-ray diffraction (SC-XRD) studies will be presented, together with theoretical calculations for atomic charges to rationalize the reactivity of R_2btp ligands. The magnetic behaviour of **4a** with its solvent-dependent SCO properties and powder X-ray diffraction experiments for phase transition will be also reported.

Results and Discussion

Synthesis and X-Ray Crystal Structures of the Ligands

The two ligands Me_2btp and tBu$_2$btp could be suitably synthesized by alkylation of H_2btp.[36,37] Its reaction with *t*BuOH led to the selective alkylation of the tetrazole rings in the *N*2 position due to steric hindrance of *t*Bu groups, while in the case of the reaction with the less-hindered methyl iodide, mixture of the three *N*1,*N*1, *N*1,*N*2 and *N*2,*N*2 possible isomers had to be separated by column chromatography, but the desired *N*2,*N*2-Me_2btp ligand could be isolated in acceptable yield.[33] We obtained crystals suitable for SC-XRD studies of both ligands from evaporation of polar solvents and their molecular structures are depicted in Figure 1. They crystallize in the monoclinic crystal system, even if in different space groups (Table S1). They give rise to peculiar crystal packing in the solid state according to the different steric occupancy of methyl *vs tert*-butyl group. In addition to their different steric hindrance, the presence of methyl *vs tert*-butyl groups imparts a different solubility to the ligands with important consequences in the reactivity studies highlighted in the following discussion.

Molecules of Me_2btp are not perfectly planar with mutual rotation between the pyridyl and tetrazolyl least squares (l.s.) planes of 9.25°. They are aligned in parallel chains along the *b* axis forming 2D layers with a net of intermolecular contacts within the plane involving the methyl group and both the pyridyl (C3(H3)···C5 = 3.785(3) Å) and the tetrazolyl (C5(H5 C)···N3 = 3.444(3) Å) rings. Layers are then packed each other with an interlayer distance of 3.215 Å, where the methyl group is involved in a short intermolecular contact with the nitrogen atom of the pyridyl ring (C5(H5B)···N5 = 3.544(4) Å) (Figure S1). Molecules of tBu$_2$btp present a higher planarity with respect to Me_2btp, with one tetrazolyl ring almost coplanar with the pyridyl ring (rotation angle below 1°) and the second tetrazolyl ring rotated by 7.07°. Intermolecular contacts involving C–H of the pyridyl ring in *meta* position and one tetrazolyl nitrogen atom contribute to form dimeric units (C4(H4)···N4 = 3.376(4) Å), which interact each other through another C–H···N contact involving the *t*Bu groups and another tetrazolyl nitrogen atom (C9(H9 A)···N1 = 3.644(4) Å) (Figure S2).

Reaction Conditions and Isolation of Iron(II) Complexes

Reactions of both ligands with anhydrous $FeCl_2$ under inert atmosphere were performed with both ligand:metal 2:1 and 1:1 molar ratios between R_2btp and $FeCl_2$ in DCM or tetrahydrofuran (THF), followed by crystallization from

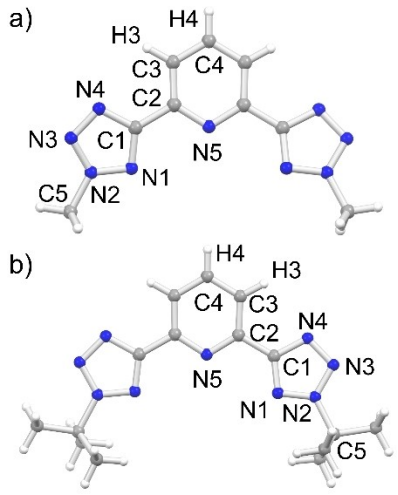

Figure 1. X-ray molecular structures of a) Me_2btp and b) tBu$_2$btp with atom numbering used in ^{1}H and ^{13}C NMR assignments; colour code: N = blue, C = grey, H = white.

Research Article
doi.org/10.1002/ejic.202400124

DCM–Et_2O (Et_2O = diethyl ether) in order to obtain crystals suitable for SC-XRD. In the case of Me_2btp, neither the ratio nor the solvent influences the obtained compound, being always **1a**·0.67DCM. When operating with tBu$_2$btp, the 1:1 ratio led to obtain **2a**·0.5Et_2O, the octahedral complex analogous to **1a**, while the 2:1 ratio drives the reaction toward **2b**, where three ligands with different coordination modes and one water molecule surround the iron(II) centre (see Scheme 1 and below for crystal structure descriptions). In all cases, the chloride is never coordinated to iron(II) even working in the 1:1 ratio, and half of the iron(II) ions were inevitably oxidized to iron(III), and the driving force of all the reactions can be sought after the formation of the tetrachloroferrato anion. In fact, this oxidation was never observed with the anion ClO_4^- even in the presence of oxygen (see discussion below). In the case of **2b**, the excess of ligand left after the partial oxidation to $FeCl_4^-$ could have also favoured the obtained species, even if we already observed the delicate energy balance among the coordination of Me_2btp and solvent molecules to iron(II).[33]

We then exchanged the iron(II) chloride salt with the perchlorate one to obtain complexes without a paramagnetic counterion, and being ClO_4^- among the most common non-coordinating anions used for SCO complexes.[22,38] We recently reported about the solvent-incorporating octacoordinated complex **3b**·H_2O as trapped intermediate in the conversion of the red crystals of the mixed HS/LS derivative **3a** into **3a**·**3c** from the reaction of Me_2btp with $Fe(ClO_4)_2 \cdot 6H_2O$.[33] Repeating the reaction with the ligand tBu$_2$btp, we could obtain well-formed yellow needle-like crystals of **4a**·4DCM by slow diffusion of Et_2O into the DCM solution of the complex obtained by reaction of the ligand with $Fe(ClO_4)_2 \cdot 6H_2O$ in CH_3CN and then evaporating the solvent and re-dissolving the residue in DCM (Scheme 1). Noteworthy, the formation of few red crystals could be observed in solution in the early stages of the crystallization, but they revealed to be unstable and quickly transform into the yellow needles upon progressing of the solvent diffusion. Those red crystals can be speculatively assigned to the initial formation of a mixed HS/LS derivative analogous to **3a**. Crystallization attempts from liquid diffusion of Et_2O into

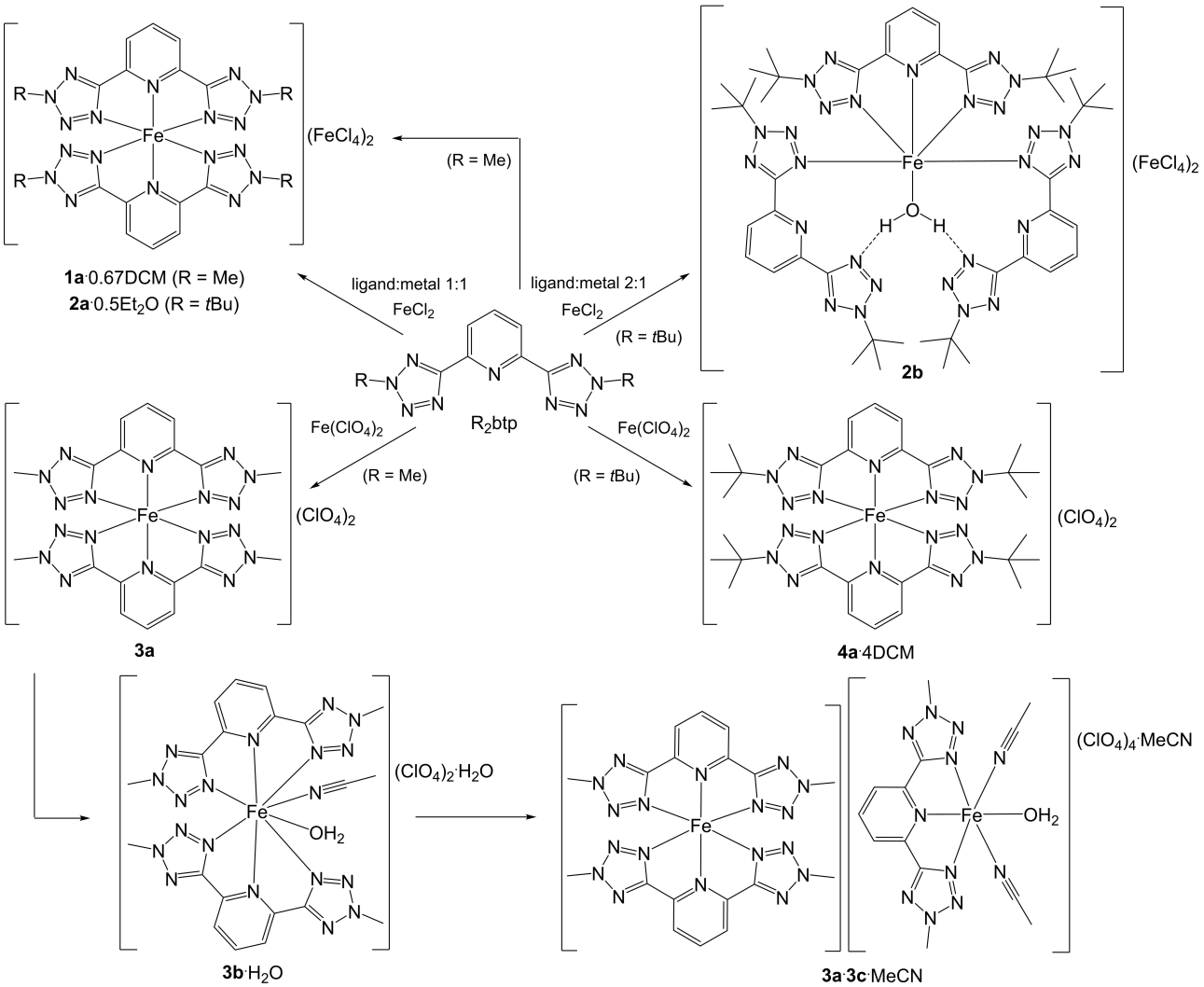

Scheme 1. Reaction scheme of R_2btp ligands with iron(II) salts.

Research Article
doi.org/10.1002/ejic.202400124

mixtures of DCM and MeCN in different ratios, till pure MeCN, did not address the selective formation of red crystals, always leading to mixed red-yellow amorphous solids and colourless crystals of the free *t*Bu$_2$btp ligand.

The yellow needles of **4a**·4DCM quickly faded once exposed to air due to loss of DCM molecules. The yellow powder, if not kept in the absence of air, promptly absorbed humidity from the ambient atmosphere yielding **4a**·1.5H$_2$O, as highlighted by the elemental analysis. In order to confirm the absorption phenomenon, the water content was also investigated by TG analysis, which showed a continuous weight loss of 2.88(1)% from room temperature to about 150 °C (Figure S3). Losses in low temperature range are usually given by lattice solvents,[39] and in this case corresponds to the expected value of 2.88% for 1.5 molecule of water, in perfect agreement with the elemental analysis. The dried complex started decomposing at about 180 °C, with an abrupt exothermic step at 200 °C (Figure S3).

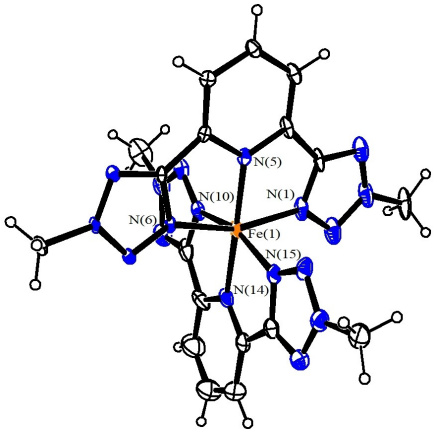

Figure 2. View of the molecular structure of the dication of **1a**·0.67DCM; displacement ellipsoids are at the 30% probability level; colour code: Fe = orange, N = blue, C and H = white; anions $FeCl_4^-$ and solvent molecules omitted for clarity (see Table 1 for distances and angles).

X-Ray Crystal Structures of 1a·0.67DCM, 2a·0.5Et$_2$O, 2b and 4a·4DCM

The complexes **1a**·0.67DCM, **2a**·0.5Et$_2$O and **2b** could be isolated as well-formed red-orange crystals, while **4a**·DCM crystallizes as long yellow needles. All crystals were suitable for SC-XRD studies, and their structures are reported in Figures 2, 3, S4 and S5, together with main bond distances and angles in Table 1 and Figure 3. The suitable single crystal of **4a**·4DCM needed to be rapidly frozen under the nitrogen stream of the diffractometer to avoid fading to amorphous powder (see above), so the crystal structure could be achieved only at 100 K. Notably, no colour change occurred upon cooling, first hint that the complex probably remains blocked in its HS state, usually characterized by the yellow colour.[33,40] The crystal structure of **1a**·0.67DCM was also determined only at 100 K due to loss of solvent upon warming toward room temperature, even if the crystals were less delicate than **4a**·4DCM. The ether molecule is instead stably packed in the crystals of **2a**·0.5Et$_2$O so the structure could be achieved at 293 K.

1a·0.67DCM, **2a**·0.5Et$_2$O and **4a**·4DCM show the coordination around the iron(II) ion of two R$_2$btp molecules behaving as tridentate ligands coordinated in *mer* fashion, similarly to complexes with bpp ligands.[16] The long Fe–N bonds, r_{Fe-N} = 2.218 Å, in **4a**·4DCM confirm that the iron(II) centre is blocked in the HS state even at low temperatures, as speculated from the invariant yellow colour upon freezing at 100 K and as

Table 1. Coordination distances (Å) and angles (°), together with distortion parameters θ and Σ (°) of **1a**·0.67DCM, **2a**·0.5Et$_2$O, and **4a**·4DCM.

	1a·0.67DCM [a] (100 K)		**2a**·0.5Et$_2$O [a] (293 K)		**4a**·4DCM (100 K)
	Molecule 1	*Molecule 2* [b]	*Molecule 1*	*Molecule 2*	
Fe(1)–N(1)	1.946(10)	1.947	2.191(4)	2.180(5)	2.227(13)
Fe(1)–N(5) (py)	1.926(10)	1.937	2.164(4)	2.173(4)	2.184(12)
Fe(1)–N(6)	1.938(9)	1.948	2.147(4)	2.195(4)	2.211(13)
Fe(1)–N(10)	1.938(11)	1.930	2.210(5)	2.177(4)	2.268(14)
Fe(1)–N(14) (py)	1.928(11)	1.940	2.148(5)	2.155(4)	2.196(12)
Fe(1)–N(15)	1.978(12)	1.975	2.206(6)	2.180(5)	2.219(13)
$r_{Fe-N\ (tetrazole)}$ [c]	1.951	1.950	2.202	2.183	2.231
$r_{Fe-N\ (py)}$ [c]	1.927	1.938	2.156	2.164	2.190
N(1)–Fe(1)–N(6) (ψ_1)	160.0(5)	159.3	147.18(17)	145.68(18)	148.4(5)
N(10)–Fe(1)–N(15) (ψ_2)	160.4(5)	160.5	146.8(2)	147.40(18)	146.2(5)
N(5)–Fe(1)–N(14) (ϕ)	177.6(5)	177.7	155.09(17)	158.21(17)	161.7(5)
θ [d]	89.96	–	80.47	83.71	85.10
Σ [e]	85.3	87.3	157.4	155.1	152.9

[a] two independent cations present within the unit cell; [b] esd's absent due to the structural disorder; [c] mean Fe–N distance; [d] dihedral angle between the two ligands (the plane of each ligand was defined as the least-squares plane through its sixteen aromatic C/N atoms); [e] see ref.[38] for the definition of the parameter.

Research Article
doi.org/10.1002/ejic.202400124

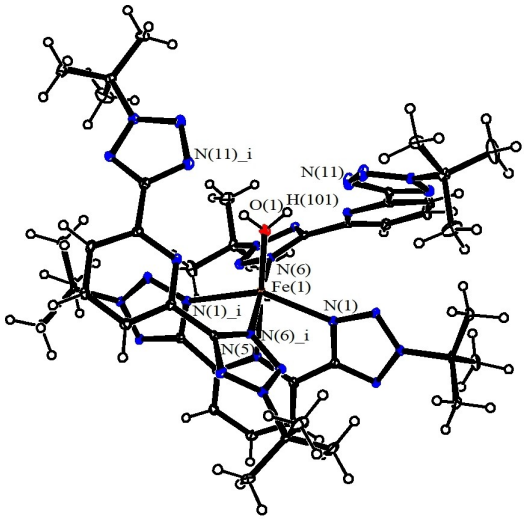

Figure 3. View of the molecular structure of the dication of **2b**; displacement ellipsoids are at the 30% probability level; colour code: Fe = orange, N = blue, C and H = white; anions $FeCl_4^-$ omitted for clarity. Symmetry transformation used to generate equivalent atoms: *y*, *x*, −*z*. Main bond distances (Å) and angles (°): Fe(1)–N(1) 2.250(3), Fe(1)–N(5) (py) 2.188(4), Fe(1)–N(6) (py) 2.244(3), Fe(1)–O(1) 1.993(4), N(1)–Fe(1)–N(1)_i (ψ_1) 146.49(16), N(6)–Fe(1)–N(6) i (ψ_2) 174.98(16), N(5)–Fe(1)–O(1) (ϕ) 180.00(7). H-bond: O(1)–H(101) 0.83(2), H(1)···N(11) 2.14(3), O(1)···N(11) 2.919(4), O(1)H-(101)N(11) 156(5).

confirmed by the magnetic measurements (see below). The angles $\phi = 161.7(5)°$ and $\theta = 85.10°$ also show how the coordination geometry of iron(II) is strongly distorted and departed from the perfect octahedron (which would require $\phi = 180°$ and $\theta = 90°$), preventing the transition by cooling, as demonstrated for compounds with bpp ligands.[19,22] The exchange of counterion from **4a**·4DCM (ClO_4^-) to **2a**·0.5Et$_2$O ($FeCl_4^-$) does lead to an even more distorted coordination of the iron(II) centre in **2a**·0.5Et$_2$O, with slightly shorter $r_{Fe-N} = 2.178$ Å compared to **4a**·4DCM, but with more pronounced deviation from octahedron of the angles $\phi = 155.09(17)/158.21(17)°$ and $\theta = 80.47/83.71°$, so as to strongly suggest an invariant HS state at all temperatures. On the other hand, **1a**·0.67DCM clearly shows distances (1.943/1.946 Å) and angles ($\phi = 177.5(5)$ and $\theta = 89.96°$) compatible with a LS state, and this suggests how R$_2$btp ligands are able to host both HS and LS iron(II) centres (Figure 4).

Differently from **1a**·0.67DCM, **2a**·0.5Et$_2$O and **4a**·4DCM, the $[Fe(t^3Bu_2btp\text{-}\kappa^3N,N',N'')(tBu_2btp\text{-}\kappa N)_2(H_2O\text{-}\kappa O)]^{2+}$ cation of **2b** contains one tridentate *t*Bu$_2$btp, two monodentate *t*Bu$_2$btp (bonded via the N(4) of one of the two tetrazolyl rings) and one H$_2$O molecule. The iron(II) centre of the cation is located on a 2-fold axis and displays a distorted octahedral geometry. An intramolecular H-bond is present, involving the coordinated water molecule and the N(11) atom of the second tetrazolyl ring of the monodentate *t*Bu$_2$btp ligand. The bonding parameters of the tridentate *t*Bu$_2$btp ligand of **2b** (Figure 3) are comparable to those of **2a**·0.5Et$_2$O and **4a**·4DCM (Table 1), and together with the other bond distances led to conclude that the iron(II) is blocked in its HS state at 100 K, suggesting the inability to undergo SCO despite the more regular octahedral environment due to the weaker ligand field. The structure of **2b** is of great interest when compared to the reactivity displayed by Me$_2$btp with $Fe(ClO_4)_2 \cdot 6H_2O$, where we could isolate the octacoordinated complex **3b**·H$_2$O able to convert into the species $[Fe(Me_2btp)(MeCN)_2(H_2O)]^{2+}$ in solution.[33] Indeed, **2b** confirms the delicate energy balance among the coordination of R$_2$btp ligands and solvent molecules.

Computational Studies on Ligands and $[Fe^{II}(R_2btp)_2]^{2+}$ Dications

To rationalize the coordination ability displayed by Me$_2$btp and *t*Bu$_2$btp, DFT calculations were performed on both the R$_2$btp ligands and the $[Fe^{II}(R_2btp)_2]^{2+}$ dications. These latter were placed in both the LS ($S = 0$) and HS ($S = 2$) states to examine the influence, if any, of the different R-substituent on the coordination geometry by comparing $[Fe^{II}(R_2btp)_2]^{2+}$ dications in the same spin state. X-ray information, in fact, cannot be used to this aim since **1a**/**3a** and **2a**/**4a** adopt LS and HS states, respectively. X-ray structural data for $[Fe(Me_2btp)_2]^{2+}$ dication in the LS state are available from the **3a**·**3c**·MeCN co-crystal.[33] The optimized geometries of the ligands reproduce within 0.01 Å the X-ray ones, while comparison of the $[Fe^{II}(R_2btp)_2]^{2+}$ geometries with those of **1a**/**3a** and **2a**/**4a** in the appropriate spin state indicates that the optimized Fe–N distances are slightly longer, on average, by up to 0.03 Å especially in the case of LS, while the comparison is more scattered in the HS (Table S2). This reflects the effect of neglecting the counterions

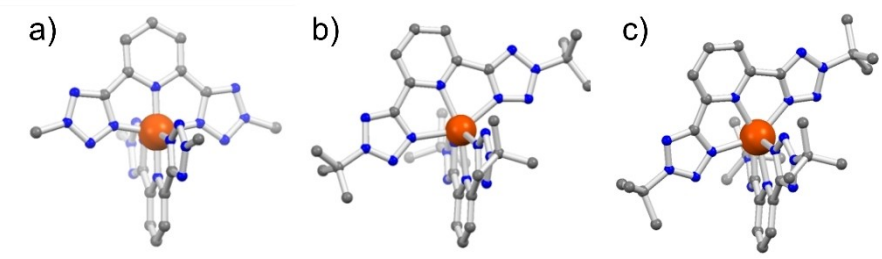

Figure 4. Perspective comparison of the $[Fe(R_2btp)_2]^{2+}$ dications in a) **1a**·0.67DCM ($FeCl_4^-$, 100 K), b) **2a**·0.5Et$_2$O ($FeCl_4^-$, 293 K) and c) **4a**·4DCM (ClO_4^-, 100 K) highlighting the distortion of the iron(II) centres and their LS or HS state; colour code: Fe = orange, N = blue, C = grey; hydrogen atoms, anions and solvent molecules omitted for clarity.

Research Article
doi.org/10.1002/ejic.202400124

in computations, but also how the counterion is critical in guiding the structural parameters, especially in the HS state.[16] Considering, however, that the error is limited, it is possible to get meaningful information on relative distances in the two dications. Calculations confirm the longer Fe–N(tetrazole) bond length with respect to the Fe–N(pyridine) one as experimentally observed in all complexes. Moreover, it is well reproduced the strong distortion of the $S=2$ geometries of both compounds from the regular octahedron.

Intriguingly, when comparing the optimized dications in the same spin state, the coordination bond lengths are essentially unvaried in the presence of Me- or *t*Bu-substituent, indicating no significant effect of such peripheric groups in the complexes. Moving to the isolated ligands, subtle but non-negligible differences are noted in the coordinating tetrazole nitrogen atoms as far as their atomic charges are considered.[41,42] In Table 2 we report the atomic natural charges for all the nitrogen atoms of Me_2btp and tBu_2btp. We note that, apart from N(2), the nitrogen atom carrying the alkyl group, the more significant difference between the two ligands is found in N(4), the coordinating tetrazole nitrogen atom. This is slightly more negative in Me_2btp with respect to tBu_2btp, denoting a greater tendency of the former to bond to the iron(II) ion with respect to the latter. Noteworthy, the highest negative charge of N(4) compared to N(1) for both ligands is in agreement with the fact that we have never observed the coordination of N(1) to iron, but always N(4). On the other hand, the formation of **2b**, instead of **2a**, when we are in excess of tBu_2btp ligand, cannot be ascribed to the greater overcrowding of tBu_2btp, since it is possible to obtain **4a**. This further strengthen the delicate energy balance among the coordination of R_2btp ligands and solvent molecules to iron(II), together with the effect of the counterion stabilizing the overall crystal packing.

Magnetic Properties of 4a

The propensity of crystals of **4a**·4DCM to quickly lose the co-crystallized solvent molecules once outside the mother liquor led to first measure its static magnetic properties on a sample of crushed crystals still immersed in the crystallization solvent into a gas-tight custom-made delrin sample holder.[43] The temperature dependence of the molar magnetic susceptibility, χ_M, is reported in Figure 5a as $\chi_M T$ *vs.* T plot. The $\chi_M T$ product remains almost constant from 300 to 100 K to a value of 3.75 emu K mol^{-1}, in accordance with a HS iron(II) centre with a significant orbital contribution,[44] as expected from the structure of **4a**·4DCM with long Fe–N distances and the high distortion of the octahedral coordination environment at 100 K.[21] Upon further cooling, the $\chi_M T$ product keeps diminishing down to 0.78 emu K mol^{-1} at 1.8 K due to the selective population of the HS state, with zero field splitting (*zfs*) effects being responsible for the final abrupt $\chi_M T$ drop at very low temperature.

A sample of **4a**·4DCM was then pumped under vacuum for several hours to remove all the co-crystallized DCM, leading to unsolvated **4a** as yellow powder. The $\chi_M T$ *vs.* T plot changed completely (red profile in Figure 5b, ***sample 1***) and upon cooling from room temperature a partial spin change of about 60% of the iron(II) centres occurs at $T_{1/2\downarrow}=187$ K, with stabilization around 100 K at 1.61 emu K mol^{-1}. This $\chi_M T$ product remains almost constant down to 50 K, where the final drop due to *zfs* effects starts till reaching 0.65 emu K mol^{-1} at 1.8 K. While heating up back to room temperature, we can observe the opening of an irregular hysteresis loop with at least three different steps (tentatively global $T_{1/2\uparrow}=206$ K). The measurement was then repeated on a new sample of **4a** keeping the lowest possible contact with air after vacuum pumping (blue profile in Figure 5b, ***sample 2***). Again we can observe the spin transition at $T_{1/2\downarrow}=194$ K with a plateau at 1.40 emu K mol^{-1} around 150 K, symptom that this time about two third of the

Table 2. Selected M06/6-311+G(d) atomic natural charges, q (*e*), of Me_2btp and tBu_2btp.[a]

	Me_2btp	tBu_2btp
N(1)	−0.244	−0.258
N(2)	−0.019	−0.044
N(3)	−0.046	−0.054
N(4)	−0.296	−0.277
N(5) (py)	−0.429	−0.433

[a] see atoms labelling in Figure 1.

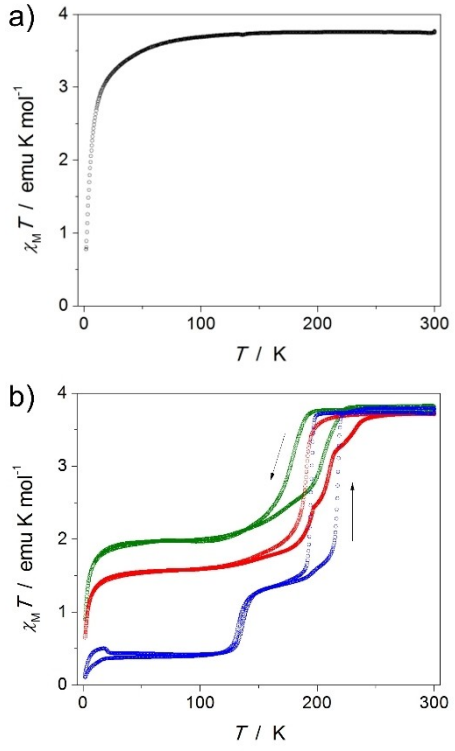

Figure 5. Temperature dependence of the $\chi_M T$ product of a) **4a**·4DCM and b) **4a** (***sample 1*** in red and ***sample 2*** in blue) and **4a**·1.5H_2O (green profile) in the 1.8–300 K range. The directions of the arrows indicate cooling and heating measurements.

Research Article
doi.org/10.1002/ejic.202400124

iron(II) centres go to the LS state, and upon further cooling below 150 K a new spin transition step occurs at $T'_{1/2\downarrow} = 135$ K, reaching a value of 0.43 emu K mol^{-1} below 120 K due to about the 90% of iron(II) centres now stabilized in the LS state while the remaining 10% is frozen in the HS state. As before, a final drop below 25 K occurs for *zfs* anisotropy. When heating up, both spin transition steps observed upon cooling give rise to hysteresis loops, a narrow one of only 2 K with $T'_{1/2\uparrow} = 137$ K, and the largest one of 23 K with $T_{1/2\uparrow} = 217$ K. These measurements highlight the dependence of the spin transition on the exposure to air of the unsolvated **4a**, and how ***sample 1*** might have suffered of air-contact with some incorporation of humidity, but also how the absence of DCM molecules within the crystal lattice modify the surrounding of the dicationic units $[Fe(t\mathrm{Bu}_2\mathrm{btp})_2]^{2+}$ so as to allow to the rearrangement of the coordination environment around the iron(II) centres and give rise to the SCO phenomenon.

The previous ***sample 2*** of unsolvated **4a** was left undisturbed to ambient conditions for few hours to test the effect of the air, and then the magnetic measurements were repeated. The $\chi_M T$ *vs.* *T* profile changes again, with the hysteresis loop still present but with lower cooperativity and only 50% of the iron(II) undergoes spin transition around 200 K. The elemental analysis and TG measurements of **4a** exposed to air already suggest the absorption of water leading to **4a**·1.5H_2O, that probably go to occupy crystal lattice positions that block half iron(II) centres in the HS state once the first half undergoes spin transition to LS state with consequent coordination rearrangement, in perfect parallelism with his congener from reaction of Me_2btp and iron(II) perchlorate.[33]

Powder X-Ray Diffraction Experiments

High-resolution powder X-ray diffraction (HR-PXRD) experiments with Synchrotron radiation were performed on the different solvates of **4a** to rationalize the structural changes (see Experimental section in the ESI for details). The ***solvated*** sample **4a**·4DCM could not be satisfactorily analysed, due to the moving of the crystals into the mother liquor with a low amount of crystals exposed to the X-ray beam. The compound suffered of decomposition at temperatures higher than 210 K, as clearly detectable from the rapid disappearance of diffraction peaks by time and the presence of black spots inside the capillary in correspondence of the incident beam. At 210 and 100 K, samples can instead sufficiently survive for the time necessary for the complete HR experiments thus allowing to register reasonable diffraction patterns with peaks at 2θ lower than 18° (Figure 6), while the bump visible at around 17° of 2θ is due to the capillary.

Comparing the patterns at 100 and 210 K, for ***dry*** sample **4a** some subtle but clear changes are evidenced. The difference in positions, shapes, and numbers of peaks highlights the occurring of the structural change upon spin transition from HS (210 K) to LS (100 K). On the contrary for the ***hydrated*** sample the high and low *T* spectra are practically identical (with only a slight shift of the peaks caused by the temperature change and consequent contraction of the unit cell at 100 K compared to 210 K), meaning that it is probably blocked in the HS state. Unfortunately, the small number of diffraction peaks did not allow structural determination, but from a qualitative point of view the spectra of the ***dry*** and ***hydrated*** samples show significant differences, indicating that the structure and the crystal packing of the iron(II) complexes are different, supporting the observed different magnetic behaviour.

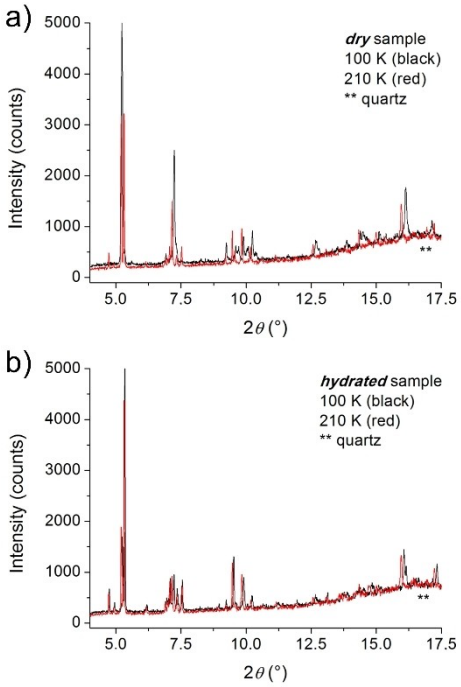

Figure 6. PXRD spectra in the 4.0–17.5° range of 2θ of a) ***dry*** and b) ***hydrated*** samples of **4a** measured at 100 (black line) and 210 (red line) K.

Conclusions

The reactivity of R_2btp ligands toward iron(II) salts has been here valorised looking for new SCO active complexes or catalytic species, revealing how the expectations can be sometimes constructively disillusioned. In fact, the chloride anion was never retained as ligand on the metal centre, and the R_2btp seems to have a higher affinity toward iron(II). The different R groups, in combination with the anion, show also a prominent effect in selecting the isolated species, going from the complexes with two *mer*-coordinated tridentate ligands **1a**, **2a** and **4a**, to the more 'exotic' species **2b** with mono- and tridentate ligands and one coordinated water molecule, strengthening the delicate energy balance among the coordination of R_2btp and solvent molecules to iron(II). These ligands are then a surprise for their variegate reactivity, and the stabilization of different species can be exploited for potential future applications. Furthermore, to the best of our knowledge, **4a** is the first iron(II) complex with this kind of ligands able to undergo SCO, so we are aiming to further explore these systems to better

Research Article
doi.org/10.1002/ejic.202400124

understand the peculiarities conferred by the peripheral tetrazolyl rings.

Experimental Section

General Information

All reagents and solvents were of reagent grade and used as received. Petroleum ether (PE) was the fraction with boiling range 40–60 °C. Elemental analyses were recorded using a Carlo Erba EA1110 CHNS–O automatic analyser. ^{1}H and ^{13}C NMR spectra were recorded at 298 K on Varian Mercury Plus VX400 (^{1}H, 399.9; ^{13}C, 100.6 MHz) spectrometer. Proton and carbon chemical shifts are given in parts per million (ppm) versus external TMS and were determined by reference to the solvent residual signals (^{1}H NMR: 7.26 ppm, ^{13}C NMR: 77.0 ppm for $CHCl_3$); coupling constants are given in Hz. Infrared spectra were recorded as KBr discs using a Jasco FTIR-4700LE spectrophotometer with a 2 cm^{-1} resolution, or as ATR spectra using the previous instrument or a Perkin Elmer FTIR-IRL1600300 equipped with a diamond tip for solids and maintaining the same resolution; bands are reported as wavenumbers (cm^{-1}) together with the assignment and relative intensity (vs = very strong, s = strong, m = medium, w = weak, br = broad). Thermogravimetric (TG) analysis was performed with a Seiko SSC 5200 Instrument coupled with a TG/DTA 320 U module in static air, by using a Pt crucible, from room temperature up to 400 °C with a heating rate of 5 °C min^{-1}. H_2btp[23,24] and Me_2btp[33] were synthesized as previously reported. Details on X-ray crystal structure determinations (Table S1), powder X-ray diffraction, magnetic measurements and theoretical calculations are given in the Supporting Information (SI).

Synthesis of *t*Bu_2btp

This ligand was synthesized by adapting a methodology reported in the literature.[37] H_2btp (0.500 g, 2.32 mmol) was dissolved in *t*BuOH (25 mL, 263 mmol) and CF_3COOH (3 mL) and H_2SO_4 96 % *m*/*m* (3 mL) were added. The reaction mixture was left under stirring at room temperature for 24 h, during which the colour changed from dark brown to yellow, and then it was poured into water (50 mL). Aqueous NaOH 0.5 mol L^{-1} was added till pH > 12, the mixture was extracted with DCM (3×20 mL), the organic phase treated with $MgSO_4$ and then taken to dryness, obtaining the ligand as a white powder. Yield: 0.304 g, 40 %. Anal. (%) calcd for $C_{15}H_{21}N_9$ (327.39): C 55.03, H 6.47, N 38.50. Found: C 54.87, H 6.56, N 38.45. ^{1}H NMR (399.9 MHz, 298 K, $CDCl_3$): δ (ppm) 8.35 (d, $J_{H,H}$ = 8.0 Hz, 2H, H3), 8.04 (t, $J_{H,H}$ = 8.0 Hz, 1H, H4), 1.85 (s, 18H, CH_3). ^{13}C NMR (100.6 MHz, 298 K, $CDCl_3$): δ (ppm) 163.70 (C1), 145.31 (C2), 138.73 (C4), 123.51 (C3), 64.58 (C5), 31.74 (CH_3). FT-IR (ATR, cm^{-1}): 3096 w + 2992 m + 2938 w (νC–H), 1598 m + 1580 m (νC=N), 1413 s + 1362 m (δC–H, *t*Bu).

Synthesis of [Fe(Me_2btp-κ^3*N*,*N*′,*N*″)$_2$]($FeCl_4$)$_2$ (1 a)

This reaction was conducted under argon atmosphere, using standard Schlenk technique. Anhydrous $FeCl_2$ (5.0 mg, 0.040 mmol) and Me_2btp (19.4 mg, 0.0797 mmol) were dissolved in THF (4 mL) and the reaction mixture was stirred for 1 h at room temperature. The solvent was then removed under reduced pressure and the solid residue was dissolved in DCM (4 mL) and stratified with Et_2O (12 mL). At complete diffusion, the title compound was obtained as red-orange prisms of **1 a**·0.67DCM suitable for SC-XRD. Yield: 11.2 mg, 59.8 %. The reaction was conducted under the same conditions with $FeCl_2$ (5.2 mg, 0.041 mmol) and Me_2btp (10.1 mg, 0.0416 mmol) always obtaining **1 a**·0.67DCM. Yield: 10.2 mg, 53.4 %. Anal. (%) calcd for $C_{18}H_{18}Cl_8Fe_3N_{18}$ (937.62): C 23.06, H 1.94, N 26.89. Found: C 22.95, H 1.86, N 26.73. FT-IR (ATR, cm^{-1}): 1616 m (νC=N), 1424 s + 1362 m (δC–H, Me).

Synthesis of [Fe(*t*Bu_2btp-κ^3*N*,*N*′,*N*″)$_2$]($FeCl_4$)$_2$ (2 a)

This reaction was conducted under argon atmosphere, using standard Schlenk technique. Anhydrous $FeCl_2$ (9.5 mg, 0.075 mmol) and *t*Bu_2btp (25.1 mg, 0.077 mmol) were dissolved in THF (4 mL) and the reaction mixture was stirred overnight at room temperature. The solvent was then removed under reduced pressure and the solid residue was dissolved in DCM (4 mL) and stratified with Et_2O (12 mL). At complete diffusion, the title compound was obtained as orange prisms of **2 a**·0.5Et_2O suitable for SC-XRD. Yield: 24.7 mg, 57.7 %. Anal (%) calcd for $C_{30}H_{42}Cl_8Fe_3N_{18}$ (1142.99): C 32.58, H 3.83, N 22.80. Found: C 33.01, H 3.98, N 22.54. FT-IR (ATR, cm^{-1}): 2985 m + 2941 w (νC–H), 1606 m + 1588 m (νC=N), 1461 m + 1370 m (δC–H, *t*Bu).

Synthesis of [Fe(*t*Bu_2btp-κ^3*N*,*N*′,*N*″)(*t*Bu_2btp-κ*N*)$_2$(H_2O-κ*O*)]($FeCl_4$)$_2$ (2 b)

This reaction was conducted under argon atmosphere, using standard Schlenk technique. Anhydrous $FeCl_2$ (5.2 mg, 0.041 mmol) and *t*Bu_2btp (26.9 mg, 0.0822 mmol) were dissolved in DCM (3 mL) and the reaction mixture was stirred for 1 h at room temperature. The deep orange solution was then stratified with Et_2O (9 mL) and the title compound was obtained as yellow-orange plates suitable for SC-XRD at complete diffusion. Yield: 15.9 mg, 53.2 %. Anal. (%) calcd for $C_{45}H_{65}Cl_8Fe_3N_{27}O$ (1451.32): C 37.24, H 4.51, N 26.06. Found: C 37.15, H 4.53, N 26.12. FT-IR (ATR, cm^{-1}): 3335 br (νO–H, H_2O), 2986 m + 2938 w (νC–H), 1604 m + 1585 m (νC=N), 1461 m + 1371 m (δC–H, *t*Bu).

Synthesis of [Fe(*t*Bu_2btp-κ^3*N*,*N*′,*N*″)$_2$](ClO_4)$_2$ (4 a)

Solid $Fe(ClO_4)_2$·6H_2O (19.5 mg, 0.0765 mmol) was added to a colourless solution of *t*Bu_2btp (50.1 mg, 0.153 mmol) in acetonitrile (CH_3CN) (6 mL) obtaining a colour change to light yellow. The reaction mixture was stirred for 30 mins and then the solvent was evaporated yielding a yellow solid, which was dissolved with DCM (6 mL). The obtained yellow solution was stratified with Et_2O (24 mL) and left to slow diffusion for one week yielding the title compound as well-formed pale-yellow needles of **4 a**·4DCM suitable for SC-XRD. Once removed from the mother liquor, crystals quickly faded to a light-yellow powder due to loss of DCM. Yield: 52.0 mg, 72 %. Anal. (%) calcd for $C_{30}H_{42}Cl_2FeN_{18}O_8$·1.5$H_2O$, **4 a**·1.5$H_2O$ (936.56): C 38.47, H 4.84, N 26.97. Found: C 38.25, H 4.94, N 26.98. A batch of yellow powder was weighed (3.521 mg) and then inserted into the Pt crucible of the TG instrument. The analysis gave the following weight losses: 2.88 (20–140 °C), 91.72 (180–220 °C) (Figure S3). FT-IR (KBr, cm^{-1}): 3407 br (νO–H,H_2O), 2992 m + 2939 w (νC–H), 1620 m (νC=N), 1463 m + 1373 m (δC–H, *t*Bu), 1100 vs (νClO_4).

Supporting Information

Experimental Section (cont.); crystallographic and refinement data for Me_2btp, *t*Bu_2btp, **1 a**·0.67DCM, **2 a**·0.5Et_2O, **2 b** and **4 a**·4DCM (Table S1); Crystal packing of Me_2btp and *t*Bu_2btp (Figures S1 and S2); Thermogravimetric analysis of **4 a**·1.5H_2O

from RT up to 400 °C (Figure S3); View of the molecular structure of the dications of **2a**·0.5Et_2O and **4a**·4DCM (Figures S4 and S5); M06/6-311 + G(d) coordination distances (Å) and angles (°), together with the distortion parameter θ (°) of $[Fe^{II}(Me_2btp)_2]^{2+}$ and $[Fe^{II}(tBu_2btp)_2]^{2+}$ dications in LS ($S = 0$) and HS ($S = 2$) states (Table S2). Deposition numbers 2333079 (Me_2btp), 2334366 (tBu_2btp), 2333080 (**1a**·0.67DCM), 2333109 (**2a**·0.5Et_2O), 2333081 (**2b**), 2333082 (**4a**·4DCM) contain the supplementary crystallographic data for this paper. These data are provided free of charge by the joint Cambridge Crystallographic Data Centre https://www.ccdc.cam.ac.uk/services/structures?id=doi:10.1002/ejic.202400124 and Fachinformationszentrum Karlsruhe http://www.ccdc.cam.ac.uk/structures.

Acknowledgements

This work has been supported by *i*) the European Union – NextGenerationEU through the Italian Ministero dell'Università e della Ricerca under PNRR "Piano Nazionale di Ripresa e Resilienza" - Mission 4 "Istruzione e Ricerca" Component 2 "Dalla ricerca all'impresa", Investment 1.1, "Fondo per il Programma Nazionale di Ricerca e Progetti di Rilevante Interesse Nazionale (PRIN)". D.D. n. 104 del 2/2/2022, project title: *Biomass-derived alcohols and polyols valorization and use by dehydrogenation/hydrogenation reactions promoted by bifunctional and proton-responsive homogeneous catalysts* (ALCOVAL), codice 20225N5T5B – CUP J53D23008500006; *ii*) the National Science Centre Poland within the Opus project 2020/37/B/ST5/02735, *iii*) the Elettra Synchrotron Trieste with the approval and financing of the Proposal 20170188 entitled *Powder X-ray diffraction structural studies on solvent-responsive spin crossover iron(II) compounds* for the use of the MCX beamline, *iv*) the Royal Society of Chemistry through the RSC Research Fund grant nr. R19-0504 entitled '*Nitrogen-donor ligands for new molecular iron(II) spin crossover complexes and cobalt(II) single-molecule magnets*', and *v*) the Dipartimento di Scienze Chimiche e Geologiche of the Università degli Studi di Modena e Reggio Emilia through the Fondo Dipartimentale per la Ricerca 2020 (FDR2020). Authors would like to thank Ms. Amanda Balzi (Università degli Studi di Bologna) for the work during her Bachelor's traineeship dedicated to this research project. Open Access publishing facilitated by Università degli Studi di Modena e Reggio Emilia, as part of the Wiley - CRUI-CARE agreement.

Conflict of Interests

The authors declare no conflict of interest.

Data Availability Statement

The data that support the findings of this study are available from the corresponding author upon reasonable request.

Keywords: iron · crystal growth · tridentate ligands · solvent effects · spin crossover

[1] O. Kahn, *Molecular Magnetism*, VCH-Verlag, Weinheim, New York, **1993**.
[2] R. L. Carlin, *Magnetochemistry: With 21 Tables*, Springer, Berlin, Heidelberg; New York; Tokyo, **1986**.
[3] *Spin-Crossover Materials: Properties and Applications*, (Ed.: M. A. Halcrow) Wiley, Chichester, West Sussex, United Kingdom, **2013**.
[4] P. Gütlich, H. A. Goodwin, Eds., *Spin Crossover in Transition Metal Compounds*, Springer, Berlin; New York, **2004**.
[5] K. Kaushik, S. Mehta, M. Das, S. Ghosh, S. Kamilya, A. Mondal, *Chem. Commun.* **2023**, *59*, 13107–13124.
[6] O. Sato, J. Tao, Y.-Z. Zhang, *Angew. Chem. Int. Ed.* **2007**, *46*, 2152–2187.
[7] O. Sato, J. Tao, Y.-Z. Zhang, *Angew. Chem. Int. Ed.* **2007**, *46*, 5049–5049.
[8] H. J. Shepherd, G. Molnár, W. Nicolazzi, L. Salmon, A. Bousseksou, *Eur. J. Inorg. Chem.* **2013**, *2013*, 653–661.
[9] N. A. A. M. Amin, S. M. Said, M. F. M. Salleh, A. M. Afifi, N. M. J. N. Ibrahim, M. M. I. M. Hasnan, M. Tahir, N. Z. I. Hashim, *Inorg. Chim. Acta* **2023**, *544*, 121168.
[10] Y. Fang, Y.-S. Meng, H. Oshio, T. Liu, *Coord. Chem. Rev.* **2024**, *500*, 215483.
[11] P. Gütlich, Y. Garcia, H. A. Goodwin, *Chem. Soc. Rev.* **2000**, *29*, 419–427.
[12] M. A. Halcrow, *Chem. Lett.* **2014**, *43*, 1178–1188.
[13] D. Pinkowicz, M. Rams, M. Mišek, K. V. Kamenev, H. Tomkowiak, A. Katrusiak, B. Sieklucka, *J. Am. Chem. Soc.* **2015**, *137*, 8795–8802.
[14] F. Pointillart, X. Liu, M. Kepenekian, B. Le Guennic, S. Golhen, V. Dorcet, T. Roisnel, O. Cador, Z. You, J. Hauser, S. Decurtins, L. Ouahab, S.-X. Liu, *Dalton Trans.* **2016**, *45*, 11267–11271.
[15] V. A. Money, C. Carbonera, J. Elhaïk, M. A. Halcrow, J. A. K. Howard, J.-F. Létard, *Chem. Eur. J.* **2007**, *13*, 5503–5514.
[16] L. Marchi, S. Fantuzzi, A. Cingolani, A. Messori, R. Mazzoni, S. Zacchini, M. Cocchi, L. Rigamonti, *Dalton Trans.* **2023**, *52*, 7684–7694.
[17] M. A. Halcrow, I. Capel Berdiell, C. M. Pask, R. Kulmaczewski, *Inorg. Chem.* **2019**, *58*, 9811–9821.
[18] S. Zhao, H. Zhou, C. Qin, H. Zhang, Y. Li, M. Yamashita, S. Wang, *Chem. Eur. J.* **2023**, *29*, e202300554.
[19] I. Capel Berdiell, E. Michaels, O. Q. Munro, M. A. Halcrow, *Inorg. Chem.* **2024**, *63*, 2732–2744.
[20] M. A. Halcrow, *Coord. Chem. Rev.* **2009**, *253*, 2493–2514.
[21] L. J. Kershaw Cook, R. Mohammed, G. Sherborne, T. D. Roberts, S. Alvarez, M. A. Halcrow, *Coord. Chem. Rev.* **2015**, *289–290*, 2–12.
[22] N. Bridonneau, L. Rigamonti, G. Poneti, D. Pinkowicz, A. Forni, A. Cornia, *Dalton Trans.* **2017**, *46*, 4075–4085.
[23] W. G. Finnegan, R. A. Henry, R. Lofquist, *J. Am. Chem. Soc.* **1958**, *80*, 3908–3911.
[24] J. M. McMANUS, R. M. Herbst, *J. Org. Chem.* **1959**, *24*, 1462–1464.
[25] M. Duati, S. Tasca, F. C. Lynch, H. Bohlen, J. G. Vos, S. Stagni, M. D. Ward, *Inorg. Chem.* **2003**, *42*, 8377–8384.
[26] G. Wu, R. Kaneko, Y. Zhang, Y. Shinozaki, K. Sugawa, A. Islam, L. Han, I. Bedja, R. K. Gupta, Q. Shen, J. Otsuki, *J. Power Sources* **2016**, *307*, 416–425.
[27] C. A. Strassert, C.-H. Chien, M. D. Galvez Lopez, D. Kourkoulos, D. Hertel, K. Meerholz, L. De Cola, *Angew. Chem. Int. Ed.* **2011**, *50*, 946–950.
[28] E. S. Andreiadis, D. Imbert, J. Pécaut, R. Demadrille, M. Mazzanti, *Dalton Trans.* **2012**, *41*, 1268–1277.
[29] A. Klein, A. Krest, S. Nitsche, K. Stirnat, M. Valldor, *Eur. J. Inorg. Chem.* **2013**, *2013*, 2757–2767.
[30] J.-H. Liu, X.-Q. Guo, Z.-C. Wang, L.-X. Cai, L.-P. Zhou, C.-B. Tian, Q.-F. Sun, *Dalton Trans.* **2022**, *51*, 3894–3901.
[31] D. Gentili, N. Demitri, B. Schäfer, F. Liscio, I. Bergenti, G. Ruani, M. Ruben, M. Cavallini, *J. Mater. Chem. C* **2015**, *3*, 7836–7844.
[32] K. Senthil Kumar, I. Šalitroš, B. Heinrich, O. Fuhr, M. Ruben, *J. Mater. Chem. C* **2015**, *3*, 11635–11644.
[33] L. Rigamonti, L. Marchi, V. Fiorini, S. Stagni, S. Zacchini, D. Pinkowicz, K. Dziedzic-Kocurek, A. Forni, F. Muniz Miranda, R. Mazzoni, *Dalton Trans.* **2024**, *53*, 3490–3498.
[34] F. Moccia, L. Rigamonti, A. Messori, V. Zanotti, R. Mazzoni, *Molecules* **2021**, *26*, 2728.
[35] G. J. P. Britovsek, M. Bruce, V. C. Gibson, B. S. Kimberley, P. J. Maddox, S. Mastroianni, S. J. McTavish, C. Redshaw, G. A. Solan, S. Strömberg, A. J. P. White, D. J. Williams, *J. Am. Chem. Soc.* **1999**, *121*, 8728–8740.
[36] M. Attolini, T. Boxus, S. Biltresse, J. Marchand-Brynaert, *Tetrahedron Lett.* **2002**, *43*, 1187–1188.

Research Article
doi.org/10.1002/ejic.202400124

[37] C. Femoni, S. Muzzioli, A. Palazzi, S. Stagni, S. Zacchini, F. Monti, G. Accorsi, M. Bolognesi, N. Armaroli, M. Massi, G. Valenti, M. Marcaccio, *Dalton Trans.* **2013**, *42*, 997–1010.
[38] M. A. Halcrow, *Chem. Soc. Rev.* **2011**, *40*, 4119.
[39] L. Rigamonti, C. Cotton, A. Nava, H. Lang, T. Rüffer, M. Perfetti, L. Sorace, A.-L. Barra, Y. Lan, W. Wernsdorfer, R. Sessoli, A. Cornia, *Chem. Eur. J.* **2016**, *22*, 13705–13714.
[40] R. Kulmaczewski, F. Bamiduro, N. Shahid, O. Cespedes, M. A. Halcrow, *Chem. Eur. J.* **2021**, *27*, 2082–2092.
[41] L. Rigamonti, M. Rusconi, A. Forni, A. Pasini, *Dalton Trans.* **2011**, *40*, 10162.
[42] L. Rigamonti, A. Forni, M. Sironi, A. Ponti, A. M. Ferretti, C. Baschieri, A. Pasini, *Polyhedron* **2018**, *145*, 22–34.
[43] M. Arczyński, J. Stanek, B. Sieklucka, K. R. Dunbar, D. Pinkowicz, *J. Am. Chem. Soc.* **2019**, *141*, 19067–19077.
[44] J. Elhaïk, D. J. Evans, C. A. Kilner, M. A. Halcrow, *Dalton Trans.* **2005**, 1693–1700.

Manuscript received: March 4, 2024
Revised manuscript received: March 24, 2024
Accepted manuscript online: March 26, 2024
Version of record online: April 19, 2024